Chaos, Solitons and Fractals 186 (2024) 115209

Contents lists available at ScienceDirect

Chaos, Solitons and Fractals

journal homepage: www.elsevier.com/locate/chaos

Effect of electric field chirality on the unpinning of chemical waves in the Belousov–Zhabotinsky reaction

Anupama Sebastian [a,1], Puthiyapurayil Sibeesh [a,1], S.V. Amrutha [a,b], Shreyas Punacha [a,c], T.K. Shajahan [a,*]

[a] Department Of Physics, National Institute of Technology Karnataka, Surathkal, Mangalore, 575025, Karnataka, India
[b] Department Of Chemistry and Biochemistry, Florida State University, Tallahassee, 32304, FL, USA
[c] Department Of Oral Health Sciences, School of Dentistry, University of Washington, Seattle, 98195, WA, USA

ARTICLE INFO

Keywords:
The Belousov–Zhabotinsky reaction
Circularly Polarized Electric Field (CPEF)
Unpinning
Spiral waves
Chirality

ABSTRACT

We investigate the unpinning of chemical spiral waves attached to obstacles in the Belousov–Zhabotinsky (BZ) reaction using a Circularly Polarized Electric Field (CPEF). The unpinning is quantified by measuring the angle at which the spiral leaves the obstacle. Previously, we had found that the wave can unpin when the electric field along the direction of the spiral is above a threshold value. When we apply a DC field, this condition can be satisfied for a range of spiral phases, which we call the unpinning window (UW). With a CPEF, this UW moves either along the direction of the spiral (co-rotating) or against the spiral (counter-rotating). We find that when the field is co-rotating, it can take several rotations of the spiral to get unpinned. With a counter-rotating field, the spiral always unpins during the first rotation. We analyze how unpinning with CPEF depends on the electric field's relative speed, chirality, and strength using experiments and the Oregonator model. Our work helps to understand and control chemical waves.

1. Introduction

The Belousov–Zhabotinsky (BZ) reaction is a non-equilibrium chemical process characterized by oscillations in the chemical concentrations of reactants [1–4]. Typically, it leads to the spontaneous formation of organized wave patterns [5], such as rotating spirals [6] and circular target waves [7,8] in two dimensions. When the BZ reagents are dispersed in water-in-oil microemulsions, they can also display distinctive patterns like antispirals [9] and packet waves [10]. Remarkably, the rotating spirals and target waves observed in the BZ reaction exhibit striking similarities to patterns observed in cardiac muscle [11,12], nerve tissue [13], chicken retina [14], and aggregating slime-mold cells [15,16]. All these diverse systems possess a stable resting state. They all can be activated from this resting state by a stimulus exceeding a certain threshold. The response to the stimulus is characteristic of the medium, such as action potential in nerve and muscle cells and a sudden change in chemical concentration in the chemical medium. Subsequently, they return to their original state after a period known as the refractory period. During the refractory period, the system does not respond to the stimulus. These systems are collectively known as excitable media, and the BZ reaction is a classic example of excitable medium. The BZ reaction is used in a wide range of applications, including in onboard chemical control for mobile robots [17], chemical processors [18–21], and pressure sensors [22].

Spiral patterns commonly arise in excitable media by wave break [23]. In heterogeneous media with obstacles, these rotating spirals can move toward the obstacles and rotate around their boundary. These waves are referred to as pinned spiral waves. Pinned waves are more stable and challenging to remove [24]. When the spiral pins in a physiological tissue, it causes dynamical disorders, including cardiac arrhythmia [25] and epileptic seizures [26]. Thus, many groups have devoted attention to controlling such waves [27–36]. In this context, the BZ reaction serves as a model system [37,38] for investigating wave dynamics.

The dynamics of chemical waves in the BZ reaction can be influenced by temperature [39,40], illumination [41,42], mechanical deformation [43], stirring rate [44,45] and reactant concentration [46]. Since the BZ reaction comprises charged ions, the electric field can also interact directly with the wave patterns. When a DC field is applied, the wave drifts toward the anode with a velocity component parallel to the field and a perpendicular component, determined by the chirality of the spiral [47,48]. The spiral can also drift [49,50] in the polarized electric field. The drift velocity is maximum when we use a

* Corresponding author.
E-mail address: shajahan@nitk.edu.in (T.K. Shajahan).
[1] These authors contributed equally to the work.

https://doi.org/10.1016/j.chaos.2024.115209
Received 5 May 2024; Received in revised form 11 June 2024; Accepted 24 June 2024
Available online 4 July 2024

circularly polarized electric field (CPEF) with a frequency twice that of the spiral [51]. The wave synchronizes with the field when both share similar frequencies [52] and rotate in the same direction [53]. This synchronization is utilized in experiments to control spiral turbulence in the BZ reaction [54].

The electric field is also used to unpin chemical waves pinned to obstacles in the reaction medium. Sutthiopad et al. discovered that a minimum electric field, referred to as the critical threshold, is necessary for unpinning [55]. We have found that the wave is unpinned when the component of the electric field in the direction of the spiral is equal or greater than the critical threshold [56]. When we use a circularly polarized electric field (CPEF) moving in the same direction of the spiral, unpinning depends on the strength of the applied field, the pacing ratio, and the initial phase of the spiral at the moment the field is initiated [57]. However, how the chemical wave interacts with the CPEF depends also on the direction of the spiral. Similar dependence has been observed in cardiac models [58].

In this paper, we also investigate the unpinning of chemical waves with CPEF rotating in the opposite direction of the spiral. We use the term 'counter-rotating CPEF' to distinguish the above from the previous case involving co-rotating CPEF. We employ both experiments and mathematical models to study chemical wave dynamics. We found that chirality plays a significant role in determining (1) the number of rotations before unpinning, (2) the unpinning window, and (3) the critical frequency of CPEF above which the field cannot unpin. In the next section we describe our experiments and the mathematical model used in this paper. Section 3 contains our main results. Further results are also listed in the appendix. In Section 4 we conclude with a discussion of our results.

2. Methods

2.1. Experimental methods

The experiments were performed as described in Amrutha et al. [57]. The concentrations of reagents we used were [H_2SO_4] = 0.16 M, [$NaBrO_3$] = 40 mM, [Malonic acid] = 40 mM, and [Ferroin] = 0.5 mM. We prepared the stock solutions using deionized water and embedded the reaction mixture in 0.8% w/v agar-agar gel. Once one color oscillation was observed, the reaction mixture was transferred to a Petri dish with a diameter of 10 cm. An oxidation wave was induced at the center on the Petri dish's surface by touching it with a silver wire during gelation. Breaking the above wavefront generated a pair of oppositely rotating spirals.

A glass bead of radius 0.6 mm, which acts as an un-excitable obstacle, was gently placed at the tip of one of the rotating spirals. Only half of the bead is inserted into the gel to ensure that the spiral becomes pinned to the great circle of the spherical bead. The spiral period to travel the obstacle circumference, $T_s \approx 300$ s. Once the spiral is pinned to the obstacle, it becomes highly stable, with its position confined around the obstacle. This allows us to control the position of the spiral within the medium. We immersed two pairs of copper electrodes inside the Petri dish along the x and y directions, perpendicular to each other. In each pair, the distance between the electrodes was 5 cm. We positioned copper electrodes in such a way that the obstacle was at the center. We started applying the electric field to the BZ medium after the spiral had completed two rotations following its attachment to the glass bead. Sinusoidal signals were applied to both electrode pairs with a phase difference of 90^0 to generate an anticlockwise CPEF. The experiments were conducted on a thin gel surface, with a thickness (≈ 3 mm) lesser than the wavelength of the spiral (≈ 3.7 mm). This prevents the chemical wave from transforming into a three-dimensional structure. Throughout the experiment, a CCD camera systematically recorded images of the reaction medium at an interval of 0.5 s for a duration of one hour. We have used a LabVIEW-based virtual instrumentation software to simultaneously record and deliver an electric field to the reaction medium [59].

Table 1
Angle measurements and their definitions, used for quantifying spiral wave unpinning.

Angle	Description
ϕ_s	The spiral phase
ϕ_0	The spiral phase at the onset of field
ϕ_u	The angle at which spiral wave unpins
$\Delta\phi$	Angular distance the spiral travels before unpinning, $\Delta\phi = \phi_u - \phi_0$
θ_E	Angle of the electric field

2.2. Numerical methods

We used a two-variable Oregonator model [60,61] to model the BZ reaction as shown below.

$$\frac{\partial u}{\partial t} = \frac{1}{\epsilon}(u(1-u) - \frac{f v(u-q)}{u+q}) + D_u\nabla^2 u + M_u(\vec{E}\cdot\nabla u) \quad (1)$$

$$\frac{\partial v}{\partial t} = (u-v) + D_v\nabla^2 v + M_v(\vec{E}\cdot\nabla v) \quad (2)$$

Here, u and v correspond to the re-scaled, dimensionless concentration of $HBrO_2$ and catalyst (Fe^{3+}), respectively. In simulations, the diffusion coefficients of variables were $D_u = 1.0$, $D_v = 0.6$. An anticlockwise rotating CPEF with strength E and rotational period T_E was given to the medium. The electric field was implemented in model equations using an advection term $\vec{E}.\nabla u$ and $\vec{E}.\nabla v$ respectively. Despite being electrically neutral, the dynamics of $HBrO_2$ are strongly linked to the negatively charged Br^- ions in the reaction. The presence of an electric field affects both Br^- ions, thereby $HBrO_2$, as well as Fe^{3+}. Consequently, the electric field influences both u and v, similar to how Br^- and Fe^{3+} are affected by the electric field. Specifically, Br^- ions move towards the anode, while the Fe^{3+} ions move towards the cathode. This is represented in the model by introducing an ionic mobility term with the field-induced advection term for both variables. The mobility term is defined as $M_i \approx -z_i D_i$, where z_i is the charge and D_i is the diffusion coefficient of variables. This gives $M_u = 1$ and $M_v = -2$ in simulations. The model parameters were $q = 0.002$ and $f = 1.4$. The $\epsilon = 0.01$ determines the excitability of the medium.

The domain is discretized in space into 300 × 300 uniformly sized grids of $dx = dy = 0.1$ space units (s.u.). The explicit forward Euler method with a timestep of $dt = 0.0001$ time units (t.u.) was used for the temporal evolution. The coupling between the grids was provided via a five-point Laplacian operator. We introduced an un-excitable obstacle by setting D_u to 0.0001 and maintaining $u = 0$ at the start time, t = 0, within a circular region at the center of the medium. The radius of the obstacle was taken to be $r = 1.0$ s.u. The boundary of the domain and the obstacle were subjected to no flux boundary conditions using the phase-field method [62]. A pinned spiral wave was simulated in the medium with the period, $T_s = 1.77$ t.u. The electric field was introduced after the pinned spiral had completed two full rotations. The point of zero normal velocity ($\frac{\partial u}{\partial t} = 0$), satisfying $u = 0.15$ and $v = 0.0935$, was considered as the tip. The tip was tracked in each iteration to understand the dynamics. In simulations, if the spiral tip coordinate moved at least one grid space away from the obstacle surface, we considered it as unpinning.

In both experiments and simulations, we quantified the unpinning by measuring the position of the spiral tip on the obstacle, and this is then converted to an angle. The spiral phase, ϕ_s, is the angle formed by the line connecting the tip of the spiral wave to the center of the obstacle, from the positive *x-axis* in the direction of spiral rotation. We applied an electric field of strength, E, to the pinned spiral with the initial phase, $\phi_s = \phi_0$, and determined the angle at which the spiral wave detached from the obstacle as the unpinning angle, ϕ_u. The difference $\Delta\phi = \phi_u - \phi_0$ represents the angular distance the spiral traveled before unpinning. We have summarized the details of all the angle measurements used to quantify the field-spiral interaction in Table 1.

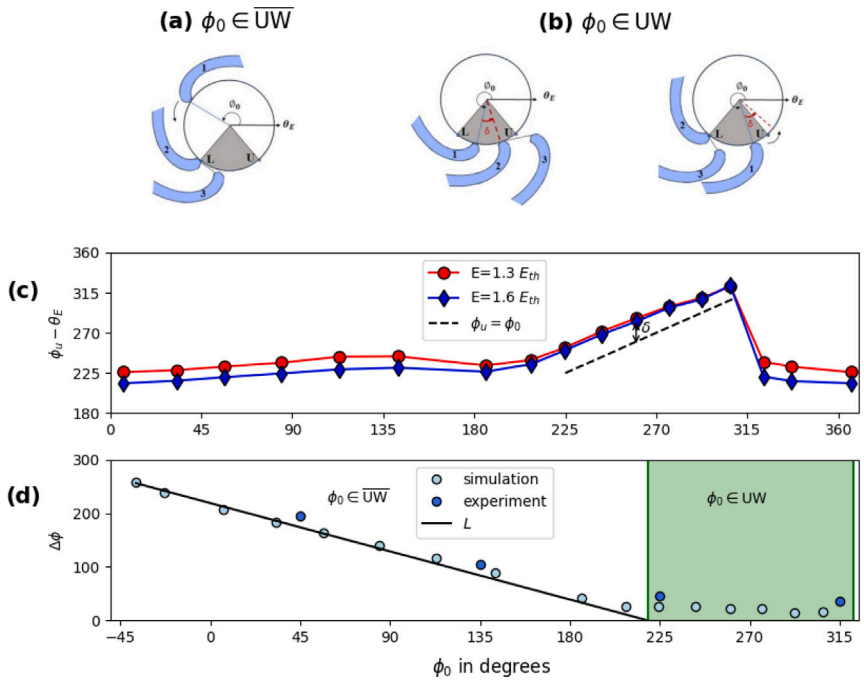

Fig. 1. Unpinning in DC electric field. A schematic of an anti-clockwise rotating spiral around an obstacle. Spirals 1, 2, and 3 correspond to the position of the spiral at three different times. The orientation of the static field is shown with the black arrow, making an angle $\theta_E = 0°$ with the *x-axis*. The unpinning window (UW) is shaded gray, where L and U correspond to the lower and upper bounds, respectively. In **(a)**, the spiral with the initial phase, $\phi_0 \in \overline{[L,U]}$ (outside the UW), unpins when it enters UW at L. In **(b)** where ϕ_0 is inside UW, $\phi_0 \in \overline{[L,U-\delta]}$, unpins after traveling δ. Otherwise, the spiral completes one more rotation and unpins at L. **(c)** $(\phi_u - \theta_E)$ *vs* ϕ_0. The unpinning angle, ϕ_u, is L and thereby stays at a fixed angle with the electric field, for all initial phases except when $\phi_0 \in [L, U-\delta]$. **(d)** $\Delta\phi = \phi_u - \phi_0$ is plotted against ϕ_0. Outside UW, $\Delta\phi$ decreases linearly with ϕ_0 at $E = 1.6\ E_{th}$. The black slanted line represents the L of UW. However, $\phi_0 \in [L, U-\delta]$ inside UW (shaded region), spiral unpins after a short delay δ.

3. Results

The spiral waves in a BZ reaction can anchor to unexcitable obstacles analogous to the pinning in the physiological tissues like the heart. Since the BZ reaction is composed of charged ions, the electric field can directly interact with the wavefront. They can be released from their anchored cores by applying an electric field of threshold field strength [55]. Chemical wave unpinning has been studied extensively using a DC electric field. We first summarize the salient features of the DC field unpinning.

3.1. Unpinning in DC electric field

Under the influence of a DC electric field of unidirectional nature, as mentioned in our previous paper [56], the unpinning happens if the component of the electric field along the spiral tangent direction, $\hat{r}_t$ equals or exceeds the critical threshold, E_{th}. Considering the above, we observed a spiral phase window that satisfies the specified condition at field strengths $E \geq E_{th}$. This window can be termed an unpinning window, UW = $[L, U]$, as depicted by the gray color in Fig. 1(a) & (b). The L and U denote the lower and upper bound of the UW when measured along the direction of the spiral rotation. The UW orient at a fixed angle with the field vector.

Since the field is static, UW also remains static with time. The spiral unpinned at the lower bound (L) as soon as it entered the UW, as shown in Fig. 1(a). When the spiral is inside the unpinning window, $L \leq \phi_0 \leq U$, the spiral was expected to unpin immediately upon applying the electric field. However, as shown in Fig. 1(b), the spiral unpinned after a short delay in its path, $\delta \approx 30°$, provided that the spiral stayed inside the UW after traveling a distance equivalent to δ. If the spiral left the UW during this delay, it rotated once again around the obstacle and unpinned at L. This is summarized in Table 2.

Fig. 1(c) shows the unpinning angle ($\phi_u - \theta_E$, with $\theta_E = 0°$ for DC field) for spirals corresponding to different ϕ_0. It was almost constant except when the spiral was within the UW. Fig. 1(d) shows the distance (in angle) the spiral moves before unpinning ($\Delta\phi = \phi_u - \phi_0$); $\Delta\phi$ decreased as the spiral got closer to the unpinning window; within the UW, $\Delta\phi \approx \delta$. Fig. 1(c) and (d) validated our mechanism portrayed in Fig. 1(a) and (b). We got similar results when we changed the direction of the spiral; shown in Appendix A.

Table 2
ϕ_u vs ϕ_0 in DC electric field.

ϕ_0	ϕ_u
$\overline{[L, U-\delta]}$	L
$[L, U-\delta]$	$\phi_0+\delta$

3.2. Unpinning with circularly polarized electric field (CPEF)

Since the spiral waves possess rotational symmetry, the application of a circularly polarized electric field (CPEF) has been used widely to control spiral drift [49,51] and turbulence [54,63]. We applied sinusoidal signals along both the x and *y-axis* with a phase difference of 90^0 between them to generate CPEF, as depicted in Fig. 2(a). This resulted in a rotating field of strength $E = \sqrt{{E_x}^2 + {E_y}^2}$ with instantaneous angle θ_E. Two additional properties characterize such a rotating field compared to the DC electric field : (1) rotational speed and (2) chirality of the CPEF. We quantified the rotational speed by the pacing ratio, $p = \frac{T_s}{T_E}$. The $p > 1$ indicates overdrive pacing where the field is faster than the spiral, $p = 1$ denotes resonance pacing where the field and the spiral move with the same speed, and $p < 1$ represents underdrive pacing where the field rotates slower than the spiral. Based on chirality, a CPEF can be of two types: 1. CPEF rotating in the direction of the spiral (co-rotating CPEF) 2. CPEF is rotating against the spiral rotation (counter-rotating CPEF). Fig. 2(b) shows unpinning by a co-rotating field in both experiments and simulation. Fig. 2(c) shows unpinning by a counter-rotating field. We discussed the salient features of these unpinning below.

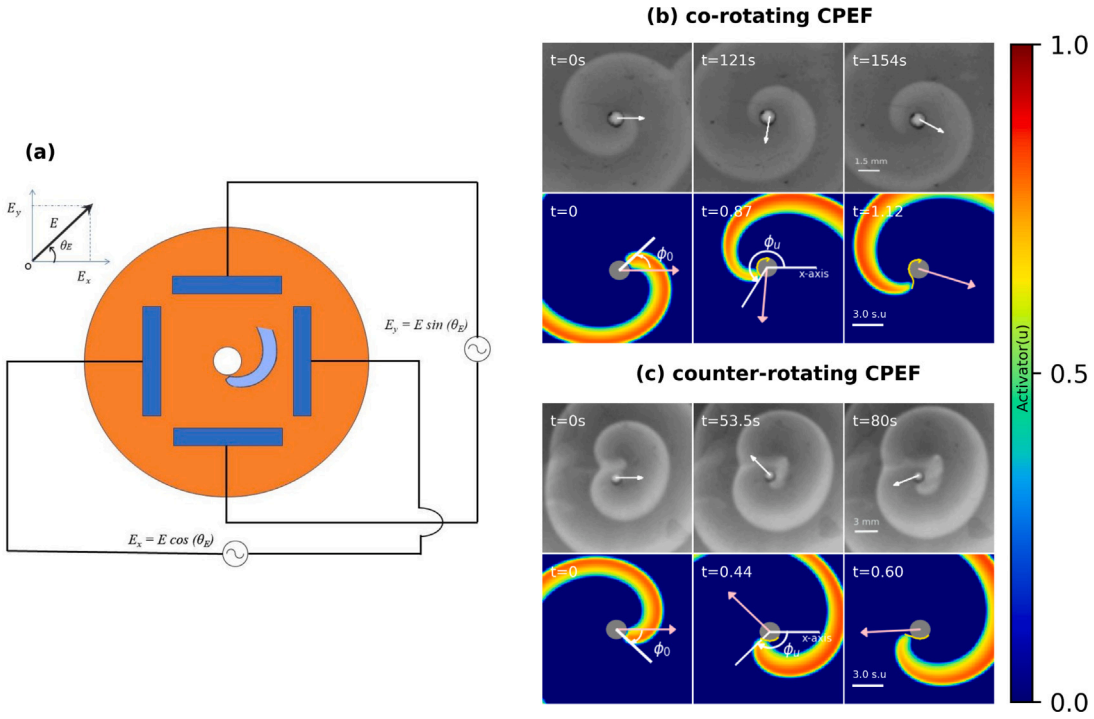

Fig. 2. Unpinning with CPEF. (a) Schematic of the experimental setup (top view). A clockwise spiral is pinned to the obstacle (white circle) at the center. The copper electrodes (blue rod) are symmetrically arranged in the four corners of the Petri dish. Two sinusoidal signals are applied across two opposite electrode pairs with a phase difference of 90°. They are $E_x = Ecos(\theta_E)$ and $E_y = Esin(\theta_E)$, with a net electric field strength, E and field angle, $\theta_E = \frac{2\pi t}{T_E}$, where T_E is the rotational period of the field. The sequences of snapshots leading to unpinning for a spiral with the initial phase, $\phi_0 = 45°$ are shown in experiment (top) and simulations (bottom). The electric field strength is $E = 1.38$ V/cm in the experiment and $E = 1.0$ in simulations; pacing ratio is 1.5 in both cases. The arrow shows the direction of CPEF. The obstacle is shown with a circle at the center of each snapshot. The CPEF is **(b)** co-rotating with the anticlockwise (ACW) spiral and the spiral unpins at $\phi_u = 229°$ when $\theta_E = 260°$. **(c)** Same as (b), but CPEF is rotating in the opposite direction. The spiral unpins at $\phi_u = 134°$ when $\theta_E = 225°$. (The angles are measured along the direction of spiral rotation.). (For interpretation of the references to colour in this figure legend, the reader is referred to the web version of this article.)

3.2.1. *Unpinning with co-rotating CPEF*

As both the spiral and electric fields rotate around the obstacle, we measured the relative phase of the spiral with respect to the electric field at unpinning, denoted as $(\phi_u - \theta_E)$ for different ϕ_0. The plot of this relative phase to ϕ_0 is shown in Fig. 3. For underdrive pacing, the mechanism is illustrated in Fig. 3(a),(b). This mechanism is the same as what happened with the DC field (Fig. 1(a), (b)), except that the unpinning window (UW) is not static. For underdrive pacing, the UW was rotating slower than the spiral; the wave entered the UW via the lower bound (L) and unpinned there. This is why Fig. 3(c) was very similar to Fig. 1(c). However, when $p > 1$, the UW moved faster than the spiral, and it met the spiral at its upper bound (U), as shown schematically in Fig. 3(d); inside UW, the spiral unpinned after δ as shown in Fig. 3(e). This explained the inverted shape of Fig. 3(f).

We examined the unpinning condition in light of our previous papers [56,57]. The equation $\vec{E} = E(cos\theta_E\hat{i} + sin\theta_E\hat{j})$ mathematically represents the co-rotating CPEF, and the spiral tip tangent vector at obstacle boundary is, $\vec{r_t} = -\sin\phi_s\hat{i} + \cos\phi_s\hat{j}$. According to the mechanism predicted by Amrutha et al., the spiral unpins when the component of the electric field along the spiral tangent direction, $\hat{r_t}$ equals or exceeds the critical threshold, E_{th} [56]. This can be expressed as $\vec{E} \cdot \hat{r_t} \geq E_{th}$. As the unpinning mechanism is different in overdrive and underdrive pacing as illustrated in Fig. 3, the above equation leads to different unpinning conditions as discussed in [57].

$$\frac{\pi + \sin^{-1}(\frac{E_{th}}{E}) - p\phi_0}{1-p} \leq \phi_s \leq \frac{2\pi - \sin^{-1}(\frac{E_{th}}{E}) - p\phi_0}{1-p}; \ (p < 1). \tag{3}$$

$$\frac{p\phi_0 + \sin^{-1}(\frac{E_{th}}{E})}{p-1} \leq \phi_s \leq \frac{p\phi_0 - \sin^{-1}(\frac{E_{th}}{E}) + \pi}{p-1}; \ (p > 1). \tag{4}$$

For $\phi_0 \in \overline{\text{UW}}$ (outside UW), ϕ_u represents the lowest point within the range of ϕ_s where the spiral reaches first (see Appendix B). Thus, the total angular path the spiral travels before unpinning, denoted by $\Delta\phi = \phi_u - \phi_0$ is given by:

$$\Delta\phi = \begin{cases} \frac{\pi+\sin^{-1}(\frac{E_{th}}{E})-p\phi_0}{1-p} - \phi_0 = \frac{\pi+sin^{-1}(\frac{E_{th}}{E})-\phi_0}{1-p}; & p < 1 \\ \frac{p\phi_0+\sin^{-1}(\frac{E_{th}}{E})}{p-1} - \phi_0 = \frac{\phi_0+sin^{-1}(\frac{E_{th}}{E})}{p-1}; & p > 1 \end{cases} \tag{5}$$

For $\phi_0 \in$ UW (inside UW), the unpinning condition is satisfied at the onset of the field. Here, the spiral unpin after a short delay ($\Delta\phi = \delta$) only if the spiral stays inside UW, even after the delay. The value of ϕ_0 that satisfy this condition can be found by solving the following equation:

$$\delta \leq \begin{cases} \frac{2\pi-\sin^{-1}(\frac{E_{th}}{E})-p\phi_0}{1-p} - \phi_0; & p < 1 \\ \frac{p\phi_0-\sin^{-1}(\frac{E_{th}}{E})+\pi}{p-1} - \phi_0; & p > 1 \end{cases} \tag{6}$$

This reduces to :

Table 3
Range of ϕ_0 that unpin after δ in co-rotating CPEF.

Co-rotating CPEF	ϕ_0 that unpins after δ
Underdrive pacing ($p < 1$)	$[L, U - \delta(1-p)]$
Overdrive pacing ($p > 1$)	$[L + \delta(p-1), U]$

In Fig. 4, we plotted $\Delta\phi = \phi_u - \phi_0$ for different ϕ_0 in experiments and simulations. This tells us how far the spiral wave traveled before unpinning since the electric field is applied, as in Fig. 1(d). The relative strength of electric field was $E = 1.6\ E_{th}$. Outside the UW, $\Delta\phi$ is a linear function of ϕ_0. The spiral unpinned at (a) L of UW in underdrive pacing with $p = 0.5$ and (b) U in overdrive pacing with $p = 1.5$. In short, unpinning occurred at the point in UW where the spiral had reached first. Inside UW (shaded region), the spiral unpinned at $\Delta\phi \approx 30^0$ for most of ϕ_0. However, if the spiral moved out of UW before this delay, it had to go for another rotation around the obstacle.

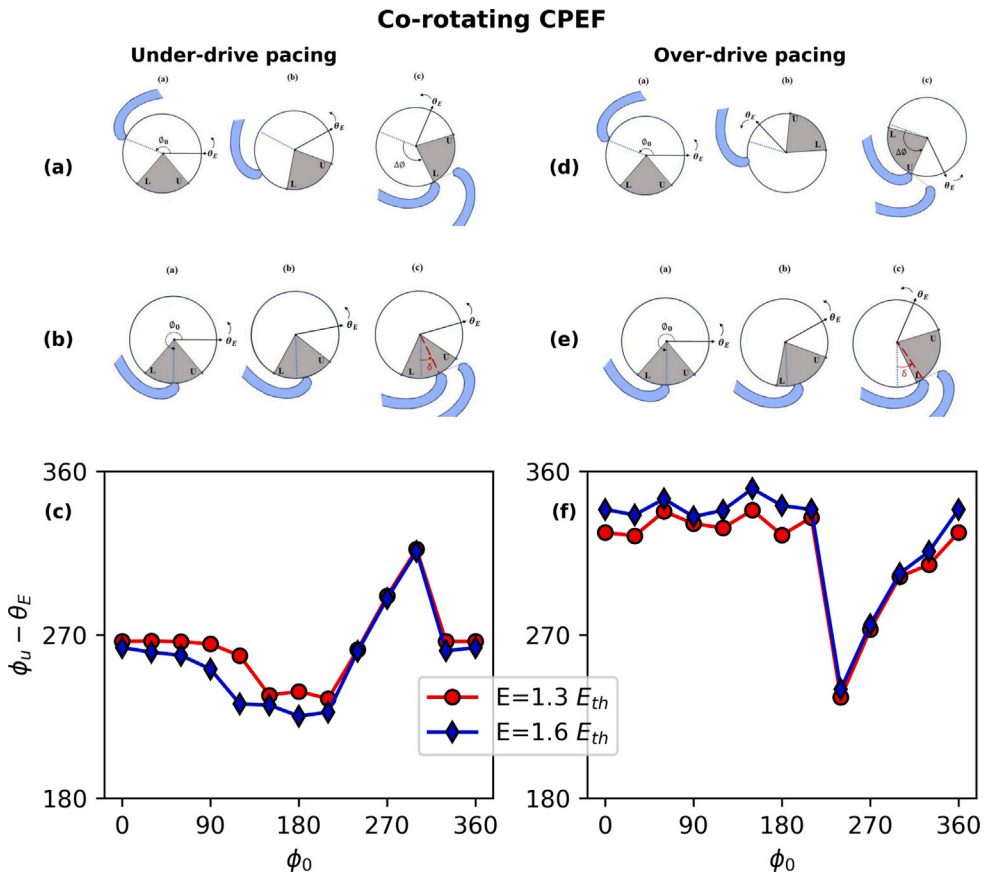

Fig. 3. Mechanism of unpinning with co-rotating CPEF. When pacing ratio is less than 1 (underdrive pacing), and for ϕ_0 outside UW, the spiral unpins at L as shown in **(a)**; but if the spiral was inside the UW, it unpins after a short delay (δ), provided it stays within the UW even after traveling δ. This is shown in **(b)**. **(c)** shows $\phi_u - \theta_E$ against ϕ_0 at $p = 0.5$ for different field strengths. This is similar to DC (see Fig. 1(c)). When the pacing ratio is greater than 1, (overdrive pacing) and outside UW, the spiral unpins at the U of UW, as shown in **(d)**. If the spiral were inside UW, it would unpin after a short delay, as shown in **(e)**. **(f)** shows the plot of $\phi_u - \theta_E$ against ϕ_0 at $p = 1.5$ (overdrive pacing).

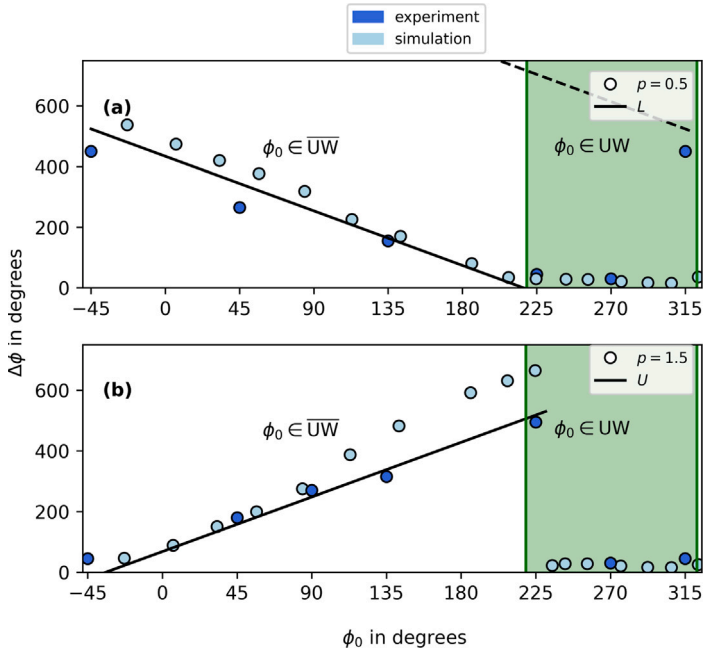

Fig. 4. $\Delta\phi$ vs ϕ_0 in co-rotating CPEF. The angular path the spiral travels before unpinning, denoted as $\Delta\phi$, is plotted for the different spiral initial phases, ϕ_0 at an electric field strength of $E = 1.6\ E_{th}$. **(a)** When CPEF has $p = 0.5$ and **(b)** $p = 1.5$. For $\phi_0 \in \overline{\text{UW}}$ (outside UW), $\Delta\phi$ is a linear function of ϕ_0. In **(a)**, the spiral unpins at L, whereas in **(b)**, it unpins at U (both represented by the slanted black line). The shaded region corresponds to the unpinning window, UW. If ϕ_0 is inside UW, the spiral unpins after a fixed delay.

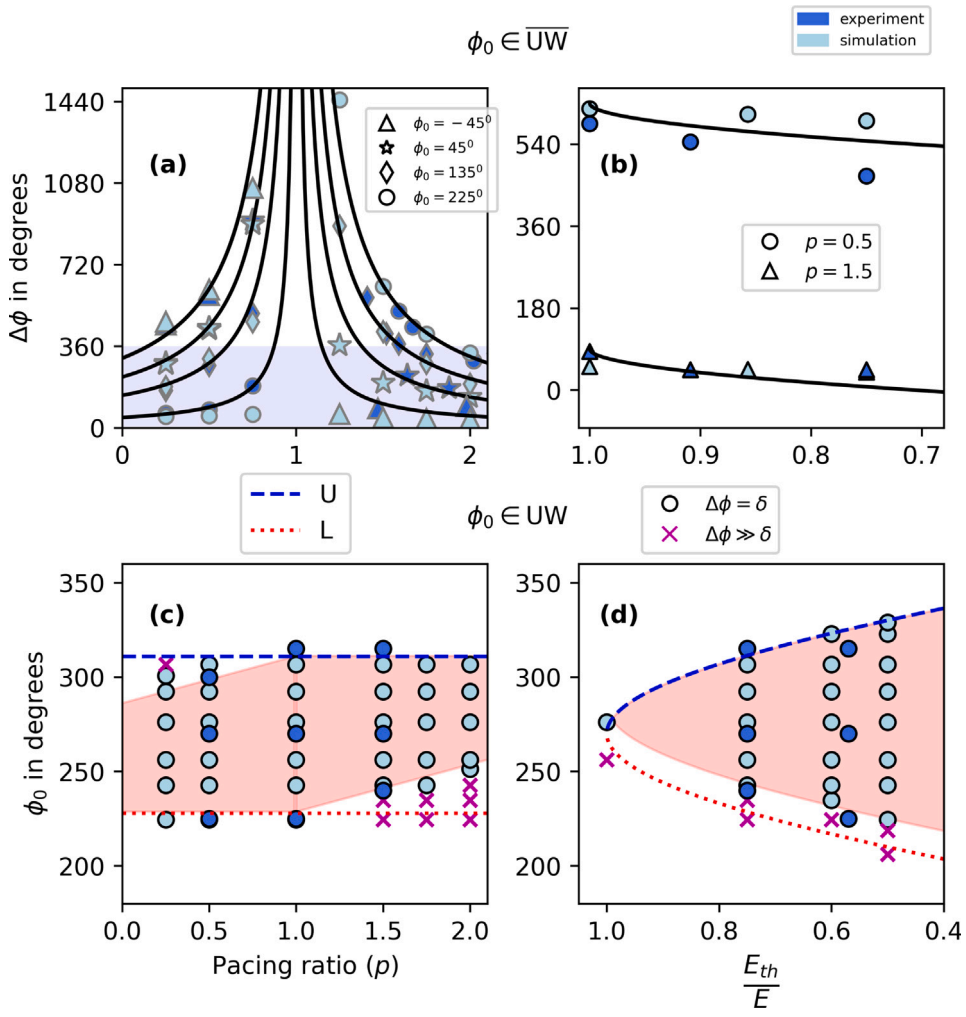

Fig. 5. Effects of p and E on spiral unpinning with co-rotating CPEF. (a) For $\phi_0 = [-45°, 45°, 135°, 225°]$ outside the unpinning window ($\overline{UW}$), the angular path the spiral travels before unpinning, denoted as $\Delta\phi$, is plotted against pacing ratio, $p \leq 2$ at $E = E_{th}$. The shaded region indicates unpinning within the initial spiral rotation. The solid lines represent theoretically predicted curves. **(b)** For a fixed $\phi_0 = -45°$, $\Delta\phi$ reduces with $\frac{E_{th}}{E}$, indicating faster unpinning with higher electric field strength. **(c)** Inside UW, the combinations of ϕ_0 and p that unpins with a short delay is marked (circles) at $E = 1.3\ E_{th}$. The remaining ϕ_0 represented with cross mark unpins in subsequent rotation when it re-enter UW. **(d)** The same is marked for different combinations of ϕ_0 and $\frac{E_{th}}{E}$ at $p = 1.5$. The blue and red lines represent the upper (U) and lower (L) bounds of UW. The range of ϕ_0 that unpins within a short delay (shaded region) varies with p and E. (For interpretation of the references to colour in this figure legend, the reader is referred to the web version of this article.)

As the unpinning window (UW) in CPEF moves along with the field vector, the unpinning angle with CPEF would also depend on the pacing ratio (p). Fig. 5(a) shows the dependence on p, for ϕ_0 outside UW. In this plot, $\Delta\phi$ was estimated at the critical threshold $E = E_{th}$. We varied the pacing ratio, p, from 0.25 to 2. We fixed the $\phi_0 = -45°, 45°, 135°, 225°$. The shaded region below $\Delta\phi = 360°$ represents unpinning within one spiral period. When the co-rotating CPEF was applied, the spiral rotated multiple times before unpinning. Fig. 5(b) shows $\Delta\phi$ as a function of field strength. It decreased with an increase in field strength, indicating that the spiral unpinned faster with higher field strength. The solid curves are theoretically estimated values from Eq. (5). Our experimental and simulation data aligned with the theoretical curve. In Fig. 5(c), we fixed the field strength at $E = 1.3\ E_{th}$, and marked all combinations of ϕ_0 and p that unpinned within a short delay δ, in experiments and simulations. The remaining ϕ_0 inside the UW unpinned in the subsequent rotation when it re-entered UW. At $p = 1$, all ϕ_0 inside UW unpinned after δ, and all spirals outside the UW have not been unpinned. Fig. 5(d) shows the same for combinations of ϕ_0 and E for a fixed $p = 1.5$. The range of ϕ_0 that unpinned within a short delay of δ widened with the field strength. The shaded region in both the above curves corresponds to the range predicted by Eq. (6) and shown in Table 3.

3.2.2. Unpinning with counter-rotating CPEF

In counter-rotating CPEF, the electric field and the spiral rotate in opposite directions. Regardless of the pacing ratio, the spiral unpinned at L of the UW, as shown in Fig. 6(a). Inside the UW, the spiral unpinned with a short delay δ, provided it remained within the UW even after traveling δ, as illustrated in Fig. 6(b). Fig. 6 also shows the relative position of the spiral to the electric field, denoted as $\phi_u - \theta_E$ for different ϕ_0 in (c) underdrive and (d) overdrive pacing. The results show that the mechanism of unpinning in counter-rotating CPEF is similar to that of DC.

When measured along the direction of spiral rotation, the equation represents the counter-rotating CPEF takes the form, $\vec{E} = E(cos\theta_E \hat{i} - sin\theta_E \hat{j})$, with spiral tip tangent vector $\vec{r}_t = -\sin\phi_s \hat{i} + \cos\phi_s \hat{j}$. The unpinning condition reduces to:

$$\frac{p\phi_0 + \pi + sin^{-1}(\frac{E_{th}}{E})}{1+p} \leq \phi_s \leq \frac{p\phi_0 + 2\pi - sin^{-1}(\frac{E_{th}}{E})}{1+p}. \tag{7}$$

For values of ϕ_0 outside of UW, $\Delta\phi$ is obtained as:

$$\Delta\phi = \frac{p\phi_0 + \pi + sin^{-1}(\frac{E_{th}}{E})}{1+p} - \phi_0 = \frac{\pi + sin^{-1}\frac{E_{th}}{E} - \phi_0}{1+p}. \tag{8}$$

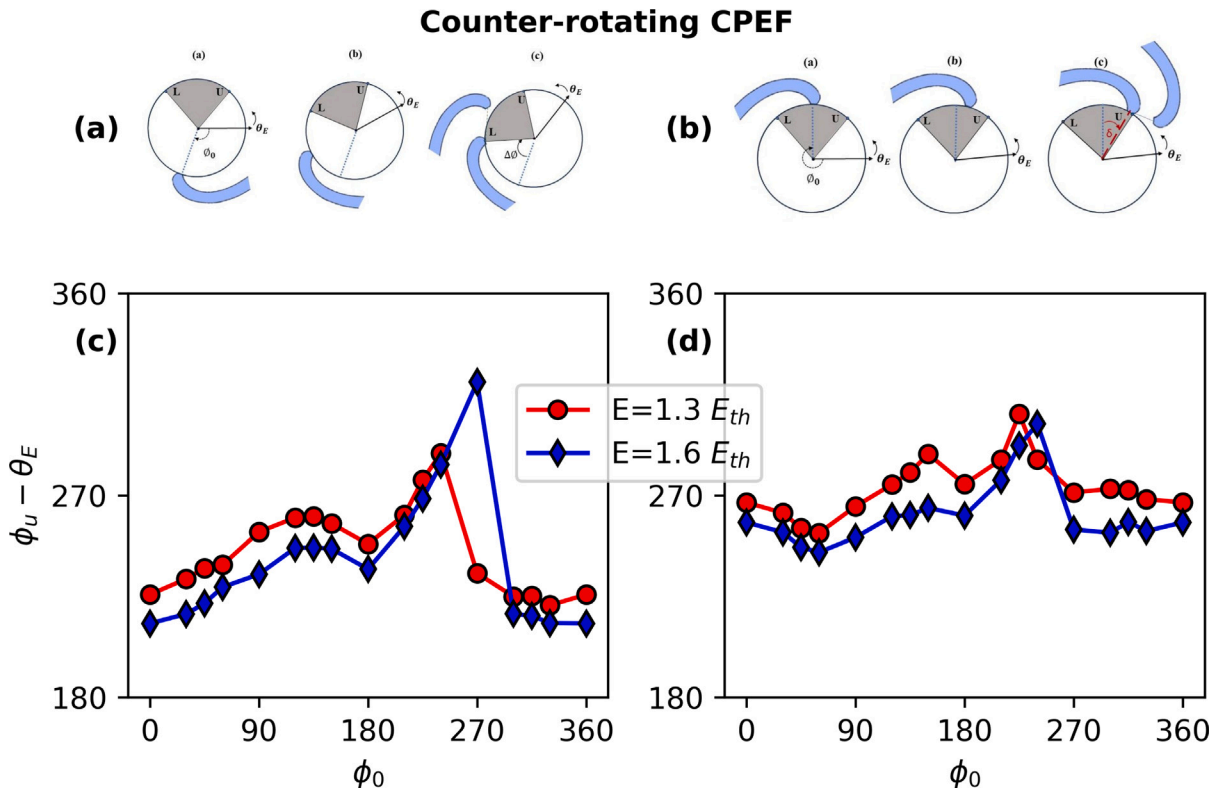

Fig. 6. Mechanism of unpinning with counter-rotating CPEF. In both overdrive and underdrive pacing, **(a)** for ϕ_0 outside UW, the spiral unpins at L of UW similar to DC. **(b)** Shows the delayed unpinning for ϕ_0 inside UW, when the spiral moves close to θ_E. The unpinning angle relative to the field vector, $\phi_u - \theta_E$, as a function of ϕ_0 at field strengths $E = 1.3\ E_{th}$ and $E = 1.6\ E_{th}$ **(c)** for underdrive pacing ($p = 0.5$), and **(d)** for overdrive pacing ($p = 1.5$).

Table 4
Range of ϕ_0 that unpin after δ in counter-rotating CPEF.

Counter-rotating CPEF	ϕ_0 that unpins after δ
$p > 0$	$[L, U - \delta(1+p)]$

Therefore, $\Delta\phi$ is a linear function of ϕ_0 with the slope being a function of p. However, when ϕ_0 is inside of UW, the range of ϕ_0 that satisfy the condition $\frac{p\phi_0 + 2\pi - sin^{-1}(\frac{E_{th}}{E})}{1+p} - \phi_0 \geq \delta$ unpin after a short delay of δ. The range of ϕ_0 is provided in Table 4.

Fig. 7 depicts the $\Delta\phi$ values estimated in experiments and simulations at a field strength of $E = 1.6\ E_{th}$ for both underdrive and overdrive pacing. Outside the UW, $\Delta\phi$ exhibited a linear relationship with ϕ_0. The spiral unpinned at L of UW in both underdrive and overdrive pacing, resembles the behavior observed in DC. The $\Delta\phi \leq 360°$ with counter-rotating CPEF; that is, unpinning happened within one rotation of the spiral. Within the UW, spirals with ϕ_0 near the lower bound (L) unpinned after a delay, while those near the upper bound (U) unpinned when it re-entered UW in subsequent rotation. This is consistent in underdrive and overdrive pacing, although the range of ϕ_0 unpinned after the short delay differed between them.

We have also studied the effect of p and E in the unpinning with counter-rotating CPEF. We systematically varied the pacing ratio and field strength for all ϕ_0, inside and outside UW. In Fig. 8(a), at field strength $E = E_{th}$ and for $p \leq 2$, most trials were inside the shaded region corresponding to unpinning within one spiral rotation. Our experimental and simulation data were in line with the theoretical curve obtained from Eq. (8). However, we observed cases where the spiral failed to unpin despite meeting the unpinning condition. For these cases, unpinning occurred in subsequent rotations, as indicated by the dotted lines, when the unpinning condition was satisfied again. Fig. 8(b) shows in counter-rotating CPEF, similar to co-rotating CPEF,

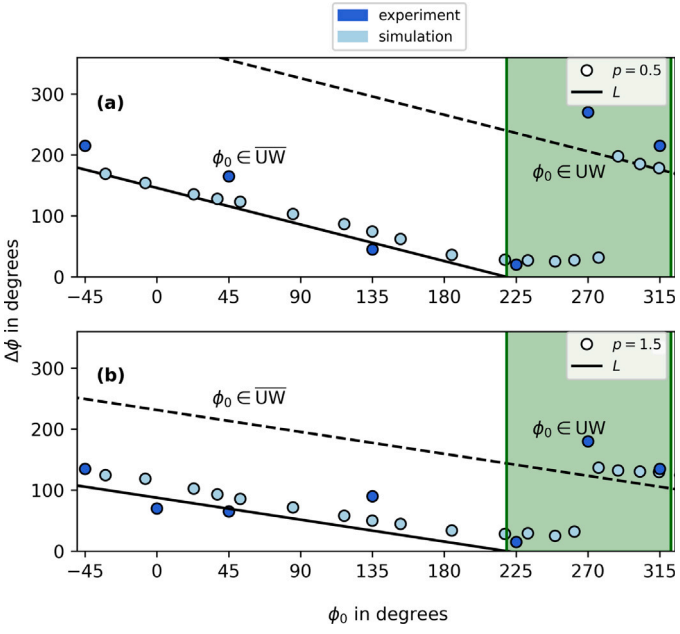

Fig. 7. $\Delta\phi$ vs ϕ_0 in counter-rotating CPEF. This is similar to Fig. 4, but when the field and spiral are in the opposite directions. However, in both **(a)** $p = 0.5$ (underdrive pacing) and **(b)** $p = 1.5$ (overdrive pacing), the slanted line represents the L of UW. The ϕ_0 inside UW, either unpin within a short delay or in subsequent rotations (dashed line).

unpinning occurred faster with increasing field strength. In Fig. 8(c) for ϕ_0 inside UW and at a fixed field strength of $E = 1.3\ E_{th}$, the range of ϕ_0 that unpinned within a short delay monotonously decreased with

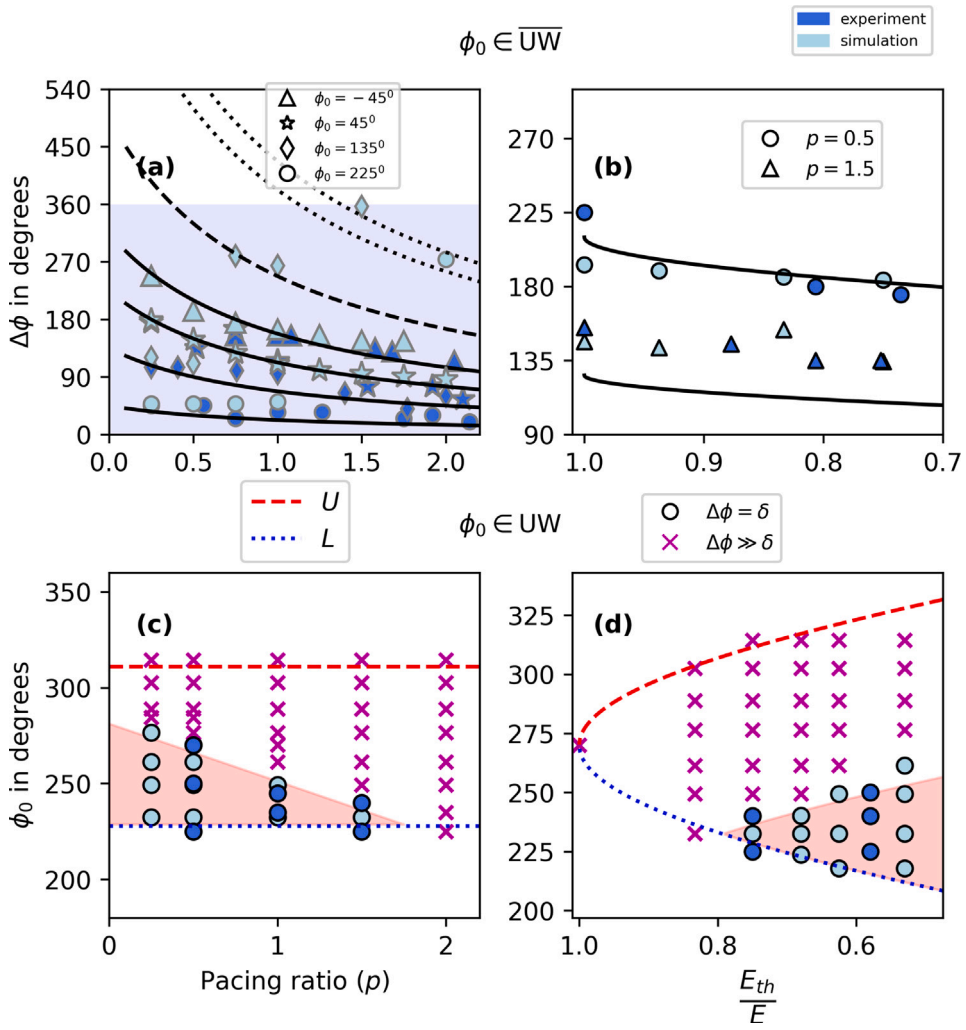

Fig. 8. Effects of p and E on spiral unpinning with counter-rotating CPEF. This is similar to Fig. 5, but when the field and spiral are rotating in opposite directions. **(a)** Most trials are unpinned within the initial spiral rotation as shown inside shaded region. **(b)** The spiral unpins earlier with increased field strength. The range of ϕ_0 that unpins within a short delay reduces **(c)** with pacing ratio (p), and **(d)** increases with E. The remaining ϕ_0 inside UW unpins in the subsequent rotation when it reaches L of UW.

the pacing ratio. At pacing ratio, $p \geq 1.75$, all ϕ_0 inside UW unpinned in the next rotation despite unpinning within a short delay. In Fig. 8(d), similar to co-rotating CPEF, the window of ϕ_0 unpinned within a short delay, widened with the field strength. However, for $E \leq 1.26\ E_{th}$, all the ϕ_0 inside UW failed to unpin within a short delay despite meeting the unpinning condition. The shaded region from plots (c) and (d) are the ranges of ϕ_0 obtained from Table 4.

3.3. Comparison between co-rotating and counter-rotating CPEF

In Fig. 9, we compared the unpinning by co-rotating and counter-rotating CPEF. We calculated how many rotations it took to unpin in each case and plotted the fraction of successful unpinning against the number of rotations it took. For this calculation, we kept $E = E_{th}$, and the initial phase was taken to be outside UW. The pacing ratio was taken from 0.25 to 1.75 in the steps of 0.25. The plot is derived from 28 experimental trials and 56 simulations. In Fig. 9(a), when co-rotating CPEF was applied, the spiral was unpinned after undergoing multiple rotations up to five. However, in Fig. 9(b), with the counter-rotating field, most trials unpinned within one spiral rotation. In experimental trials, unpinning occurred within the first rotation of the spiral for 88% of the cases. In simulations, this percentage was lower, close to 73%. However, in both the co-rotating and counter-rotating fields, few cases failed to unpin, and in these instances, the spiral rotations continued infinitely. This is represented by 'spiral rotations = ∞'. As the electric field strength increased, the percentage of unpinning during the initial rotation increased. In simulations with the counter-rotating CPEF, all cases unpinned within the initial rotation with counter-rotating CPEF at the higher electric field strength of $E = 1.3\ E_{th}, 1.6\ E_{th}$ (see Appendix C).

Inside UW, the range of ϕ_0 that unpinned within a short delay varied in both co-rotating and counter-rotating CPEF, depending on the pacing ratio. The total width of this range is represented by $\Delta\phi_0$. In the DC field, this range is given by $(\Delta\phi_0)_{DC} = U - L - \delta$. In co-rotating CPEF at a field strength of $E = 1.3\ E_{th}$, Fig. 10(a) indicates that the $\Delta\phi_0$ became wider than $(\Delta\phi_0)_{DC}$ (dotted line) when applying underdrive pacing, and overdrive pacing below $p \leq 2$. However, with Fig. 10(b) counter-rotating CPEF, $\Delta\phi_0$ was less than $(\Delta\phi_0)_{DC}$ and decreased consistently with the increase in pacing ratio. The black line corresponds to the theory curves according to Table 5.

Table 5
$\Delta\phi_0$ in various control schemes.

Control scheme	$\Delta\phi_0$
DC	$(U-L)-\delta = (\Delta\phi_0)_{DC}$
Co-rotating CPEF ($p < 1$)	$(U-L)-\delta(1-p) = (\Delta\phi_0)_{DC} + \delta\ p$
Co-rotating CPEF ($p > 1$)	$(U-L)-\delta(p-1) = (\Delta\phi_0)_{DC} + \delta\ (2-p)$
Counter-rotating CPEF ($p > 0$)	$(U-L)-\delta(1+p) = (\Delta\phi_0)_{DC} - \delta\ p$

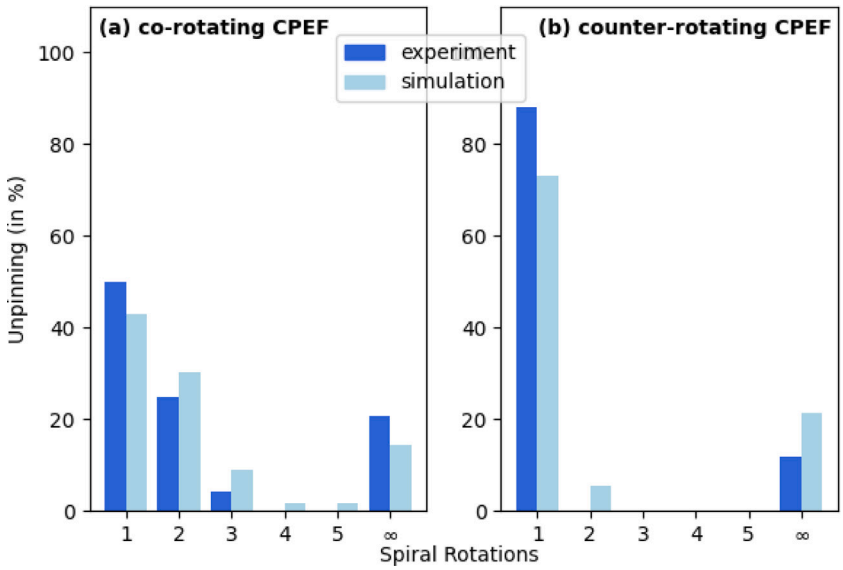

Fig. 9. Unpinning across various spiral rotations. For a range of ϕ_0 symmetrically distributed around the obstacle and $0.25 \leq p \leq 1.75$ in increments of 0.25, the percentage of unpinning is calculated for different spiral rotations (1, 2, 3, …, ∞) at electric field strength, $E = E_{th}$ for **(a)** co-rotating CPEF and **(b)** counter-rotating CPEF. The case where 'spiral rotations = ∞' indicates instances where unpinning failed. The plot is derived from 28 experimental trials and 56 simulations. Compared to co-rotating CPEF, most trials are unpinned within the first rotation of the spiral for counter-rotating CPEF.

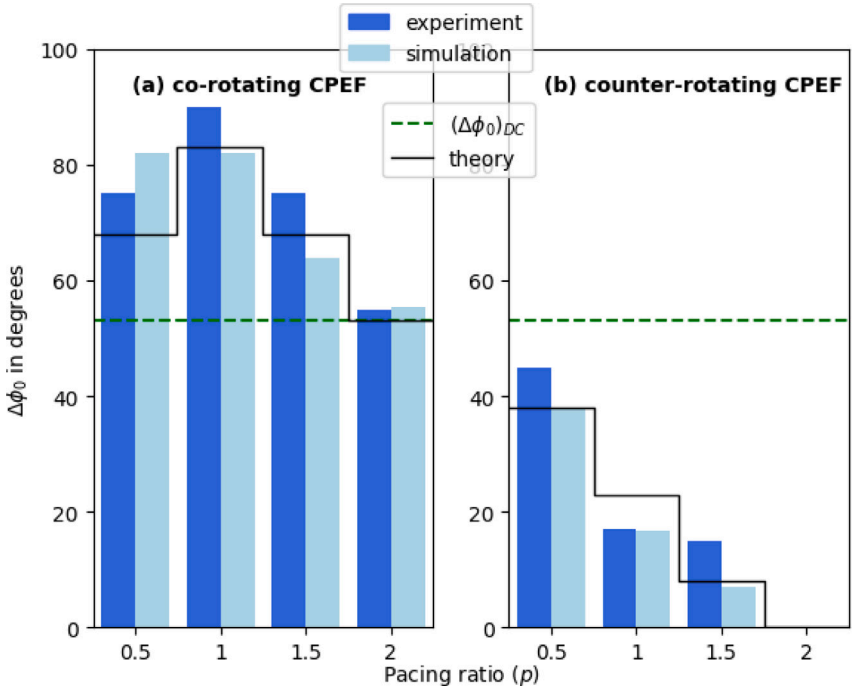

Fig. 10. Unpinning within a short delay. For ϕ_0 lying within UW, the window width of ϕ_0 that unpins within a short delay of $\delta = 30°$, denoted by $\Delta\phi_0$, is plotted against the pacing ratio $p = [0.5, 1, 1.5, 2]$ for **(a)** co-rotating CPEF and **(b)** counter-rotating CPEF. The electric field strength is $E = 1.3\ E_{th}$. The black solid line represent theoretical curves obtained from Table 5, and the green dotted line corresponds to $\Delta\phi_0$ of the DC electric field. For $p < 2$, $\Delta\phi_0$ is wider than DC for co-rotating CPEF and consistently decreased with p for counter-rotating CPEF. (For interpretation of the references to colour in this figure legend, the reader is referred to the web version of this article.)

At resonance pacing, $p = 1$, the spiral and applied field rotate at the same speed. The spiral unpins only if it enters the UW at L. For co-rotating CPEF, $(L - \phi_s)$ was invariant in time, leading to phase-locking between field and spiral. Thus, unpinning was possible only if ϕ_0 was inside UW, as shown in Fig. 11(a). However, in the case of the counter-rotating field, since the field and spiral rotate in opposite directions, the phase difference between the spiral and the field constantly changes with time. As a result, the phase-locking did not occur, and unpinning during resonance pacing was similar to underdrive and overdrive pacing, as shown in Fig. 11(b).

We tried to unpin the spiral by gradually increasing the pacing ratio in co-rotating and counter-rotating CPEF. However, the pacing ratio must be below a cutoff value, p_{cutoff}. At $E = E_{th}$ (corresponding to $\frac{E_{th}}{E} = 1$), we observed that p_{cutoff} was 3.2 in experiments and 3.5 in simulations for co-rotating CPEF. On the other hand, with counter-rotating CPEF, the experimental p_{cutoff} was 3.1, while in simulations, it was 2.1, which was lower than that of co-rotating CPEF. We then investigated the relationship between p_{cutoff} and electric field strength. Fig. 12 illustrates how p_{cutoff} increased with electric field strength in both experiments and simulations. Achieving a higher p_{cutoff} is

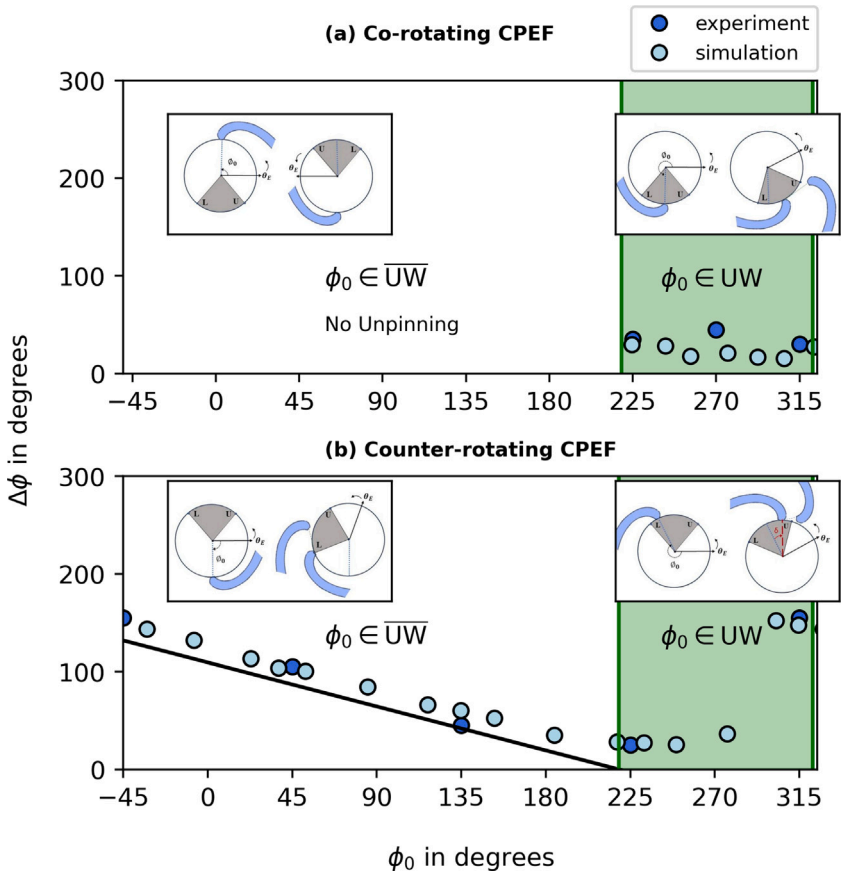

Fig. 11. Unpinning at resonance pacing ($p = 1$). A spiral subjected to resonance pacing at an electric field strength of $E = 1.6\ E_{th}$. The spiral unpins if it reaches the lower bound (L) of the unpinning window (UW). In **(a)** co-rotating CPEF, for ϕ_0 outside UW, the angular distance between L and the spiral (ϕ_s) remains constant since both the spiral and electric fields move at the same speed. Due to this phase locking, unpinning fails outside UW. However, for ϕ_0 inside UW, the spiral unpins after a short delay. In **(b)** counter-rotating CPEF, the $\phi_0 \in \overline{\text{UW}}$, unpins at L of UW. For ϕ_0 inside UW, the spiral unpins either after a short delay or upon reaching L in the subsequent rotation. In each case, the mechanism is depicted in insets.

desirable for effectively controlling the spiral wave, which is attainable at higher field strengths. However, p_{cutoff} differed among co-rotating and counter-rotating CPEF for all field strengths and was higher for co-rotating CPEF than for counter-rotating CPEF.

Our results are consistent for the spiral wave pinned to all obstacle radii, provided that the radius is greater than the spiral core radius (see Appendix D).

4. Conclusion

We investigated the unpinning of chemical waves in the Belousov–Zhabotinsky reaction using experiments and mathematical models. The spiral unpinned when the electric field component along the spiral propagation direction was equal to or exceeded the threshold field strength E_{th}. This condition is satisfied within a range of spiral phases, and we call it the unpinning window (UW). With a DC electric field, the UW remains static, and the spiral unpins immediately when it reaches the lower boundary of the UW. If the spiral initial phase is inside the UW, unpinning occurs after a short delay, provided that the spiral remains inside the UW following the delay; otherwise, the spiral unpins in subsequent rotations.

With CPEF, the unpinning also depends on the chirality and the speed of the electric field. The CPEF can be either co-rotating (rotating along a spiral direction) or counter-rotating (rotating against a spiral direction). For co-rotating electric field, and ϕ_0 outside the UW, we found that: (i) When the field is rotating slower than the spiral ($p < 1$), it unpins at the lower boundary of the UW. This is similar to the unpinning with the DC field. (ii) When $p > 1$, the spiral unpins at the upper boundary of the UW. (iii) If on the other hand, the ϕ_0 is inside the UW, the spiral unpins after a short delay. However, if the spiral leaves UW during this delay, it takes more rotations to unpin. (iv) With a counter-rotating CPEF, the wave always unpins within the initial spiral rotation around the obstacle. (v) With counter-rotating CPEF, the spiral always unpins at the lower boundary of the UW, irrespective of the pacing ratio. (vi) The range of ϕ_0 that unpins within short delay varies in both co-rotating and counter-rotating CPEF. (vii) In resonance pacing ($p = 1$), the co-rotating CPEF fails to unpin because of the phase locking between the spiral and electric field, whereas the counter-rotating CPEF always unpins. (viii) The wave can be unpinned only when the pacing ratio falls below the cutoff pacing ratio, p_{cutoff}. The value of p_{cutoff} increases with the strength of the electric field and is higher in the co-rotating CPEF than in the counter-rotating CPEF. Our results are consistent with the experiments and mathematical model.

This study is the first of its kind to explore the effect of electric field chirality on the unpinning of chemical waves, using both experimental and numerical methods. Recent studies using the CPEF have shown that the spiral can drift [51] and synchronize [52] with the field frequency when they rotate in the same direction, but not when they rotate in opposite directions. It has been found that only CPEF rotating in the opposite direction can maintain the stability of two-armed spirals, whereas CPEF rotating in the same direction tends to destabilize them [64]. This demonstrates the significance of the field chirality in spiral dynamics. In a spiral pair, the frequency and chirality of the electric field significantly affect the selection of the unique spiral direction in the medium [53,63]. Our research further confirms that the frequency (determined by the pacing ratio) and chirality of the

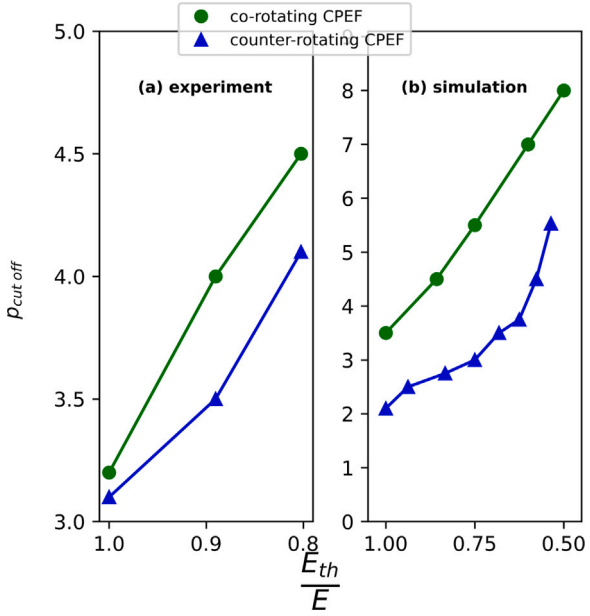

Fig. 12. p_{cutoff} **vs** $\frac{E_{th}}{E}$. In both **(a)** experiments and **(b)** simulations, the cutoff pacing ratio, $p = p_{cutoff}$ is marked against $\frac{E_{th}}{E}$. The circle corresponds to co-rotating CPEF, and triangles correspond to counter-rotating CPEF. The unpinning fails if $p > p_{cutoff}$. In co-rotating and counter-rotating CPEF, p_{cutoff} increases with electric field strength.

electric field influence the unpinning mechanism. The chemical wave can be unpinned more efficiently using a counter-rotating CPEF than a co-rotating field, as unpinning is always successful here. Moreover, with the counter-rotating CPEF, the wave can be unpinned within one rotation of the spiral irrespective of the initial position of the spiral (provided $E > E_{th}$). Thus, the counter-rotating CPEF provides an efficient method for unpinning chemical waves. However, re-pinning of the spiral to the obstacle after unpinning was faster in the counter-rotating CPEF than in the co-rotating CPEF. This needs to be investigated further.

Despite many similarities in the excitation wave dynamics, the unpinning mechanism is different in chemical and physiological excitation waves. For example, the unpinning in cardiac tissue is because of secondary excitations [27,65,66]. Punacha et al. found that the rotating frequency of the electric field must exceed a minimum cutoff frequency to unpin [58]. However, in chemical waves, the wave unpins when the field frequency is below a maximum cutoff frequency. Also, they observed that the wave was always unpinned within the first rotation of the CPEF in the cardiac model. The unpinning within the first rotation is not observed for chemical waves with the co-rotating field. Thus, one should be careful when using the results from chemical waves unpinning to cardiac waves, even though they share many striking similarities as excitation waves.

Even though the BZ reaction has been thoroughly studied in the past, interest has recently revived because of its role in many new areas, such as the self-propelled motion of droplets [67] and chemical computing [68]. In these applications, precise control of chemical waves allows us to control the system's state. Our studies are a step forward in this direction. We are able to control and predict the response of chemical waves to the electric field. We hope this will stimulate further studies and a better understanding of chemical wave dynamics and its applications.

CRediT authorship contribution statement

Anupama Sebastian: Writing – review & editing, Writing – original draft, Visualization, Software, Methodology, Data curation, Conceptualization. **Puthiyapurayil Sibeesh:** Writing – review & editing, Software, Methodology, Investigation. **S.V. Amrutha:** Methodology, Investigation. **Shreyas Punacha:** Software, Methodology. **T.K. Shajahan:** Writing – review & editing, Validation, Supervision, Resources, Project administration, Conceptualization.

Declaration of competing interest

The authors declare that they have no known competing financial interests or personal relationships that could have appeared to influence the work reported in this paper.

Data availability

Data will be made available on request.

Appendix A. Unpinning of clockwise spiral in DC electric field

See Fig. A.13.

Appendix B. Unpinning window *vs* $\frac{E_{th}}{E}$

See Fig. B.14.

Appendix C. Unpinning in various spiral rotations

See Fig. C.15.

Appendix D. Unpinning of spiral pinned to varying obstacle size

The threshold field strength (E_{th}) increases linearly with the obstacle radius, r [55]. In addition, the spiral period (T_s) increases with r [37]. Since our results are expressed in terms of $\frac{E_{th}}{E}$, $p = \frac{T_s}{T_E}$, and ϕ_0 (an angle), their form remains the same. We tested this for co-rotating and counter-rotating CPEF by varying the obstacle radius, r. The results are shown in Fig. D.16. A relatively higher electric field strength must be applied longer to unpin the spiral from a larger obstacle (as E_{th} and T_s are higher). This is evident from the comparison of (a) and (c) in co-rotating CPEF and (b) and (d) in counter-rotating CPEF. As expected, the value of ϕ_u does not vary with obstacle radius, as illustrated in (e) and (f) of Fig. D.16.

Appendix E. Supplementary data

Supplementary material related to this article can be found online at https://doi.org/10.1016/j.chaos.2024.115209.

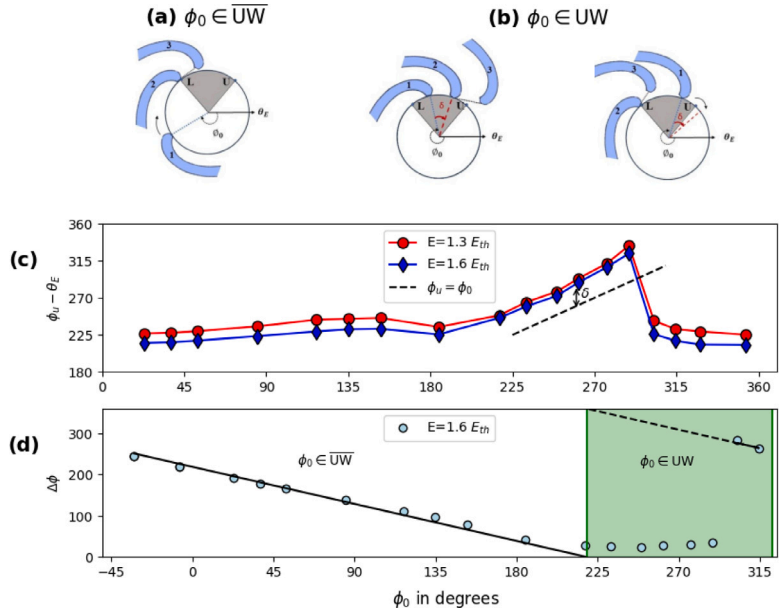

Fig. A.13. Unpinning of clockwise spiral in DC electric field. A clockwise rotating spiral is shown where 1, 2, and 3, correspond to its temporal evolution. The orientation of the static field is shown with the black arrow, with angle θ_E along the *x-axis*. The unpinning window (UW) is shaded gray, where L and U correspond to the lower and upper bounds, respectively. For ϕ_0 outside UW, the spiral unpins at L as shown in **(a)**; but if the spiral was inside UW, the $\phi_0 \in [L, U-\delta]$ unpins after a short delay (δ). If $\phi_0 \in [L, U-\delta]$, it will leave the UW, after another rotation unpins at L. This is shown in **(b)**. **(c)** $(\phi_u - \theta_E)$ *vs* ϕ_0. The unpinning angle, ϕ_u, is L and thus maintains a constant angle with respect to the electric field, which varies with field strength, except when $\phi_0 \in [L, U-\delta]$. **(d)** $\Delta\phi$ is plotted against ϕ_0. Outside the UW, $\Delta\phi$ decreases linearly with ϕ_0 at $E = 1.6\ E_{th}$. The black slanted line represents the L of UW. However, within the UW region (shaded region), for $\phi_0 \in [L, U-\delta]$, the spiral unpins after a short delay δ. We have measured the angles along the direction of spiral rotation for better comparison with Fig. 1.

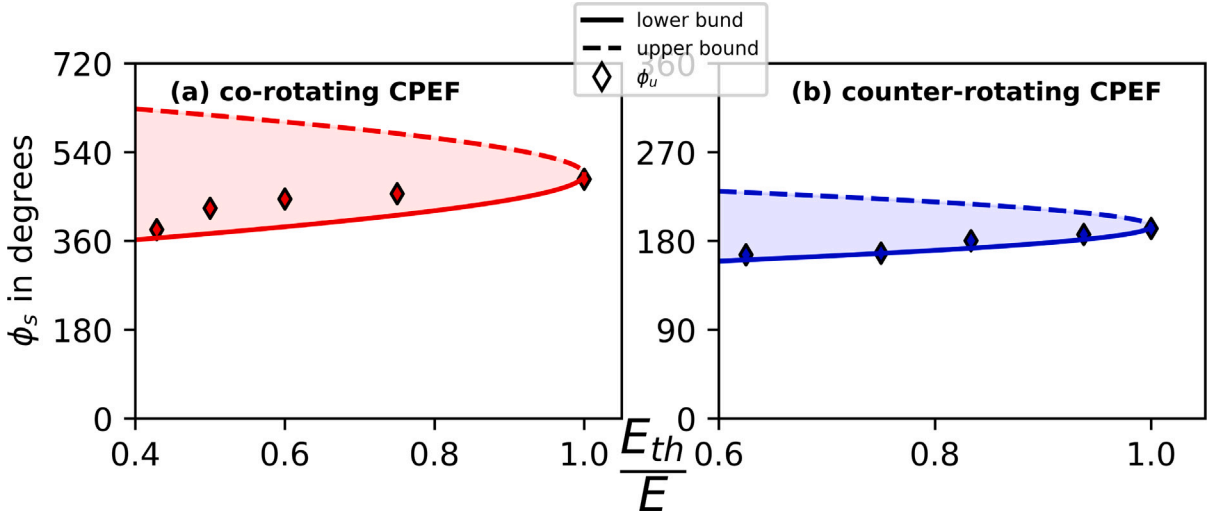

Fig. B.14. Unpinning window with $\frac{E_{th}}{E}$. For $p = 0.5$ and spiral initial phase, $\phi_0 = 45^0$ (outside UW), the unpinning angle, ϕ_u (in diamonds) is estimated by varying $\frac{E_{th}}{E}$ for **(a)** co-rotating CPEF and **(b)** counter-rotating CPEF. The shaded region is the unpinning window, where the solid and dotted lines are the lower and upper bounds of the window. Here, the lower bound corresponds to the spiral phase inside the unpinning window that the spiral reaches first during its rotation. In underdrive pacing, unpinning happens close to the lower bound of UW.

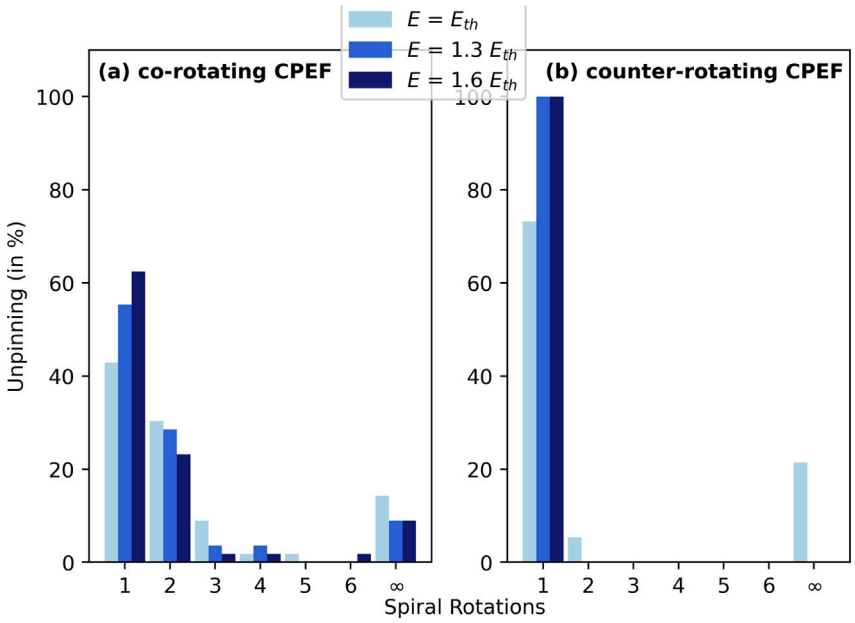

Fig. C.15. Unpinning in various spiral rotations. Out of the 56 trials, each comprising eight initial phases (ϕ_0) symmetrically distributed around the obstacle and spanning seven pacing ratios (p) from 0.25 to 1.75 in steps of 0.25, the unpinning percentage is computed for **(a)** co-rotating and **(b)** counter-rotating CPEF, across different spiral rotations (1, 2, 3, …, ∞) at three distinct electric field strengths: $E = E_{th}$, 1.3 E_{th}, and 1.6 E_{th}. The case where 'spiral rotations = ∞' corresponds to cases where unpinning failed. Across all electric field strengths, most trials unpinning within the first rotation of the spiral for counter-rotating CPEF. Notably, all cases unpinned within the initial rotation above electric field strength of $E = 1.3\ E_{th}$.

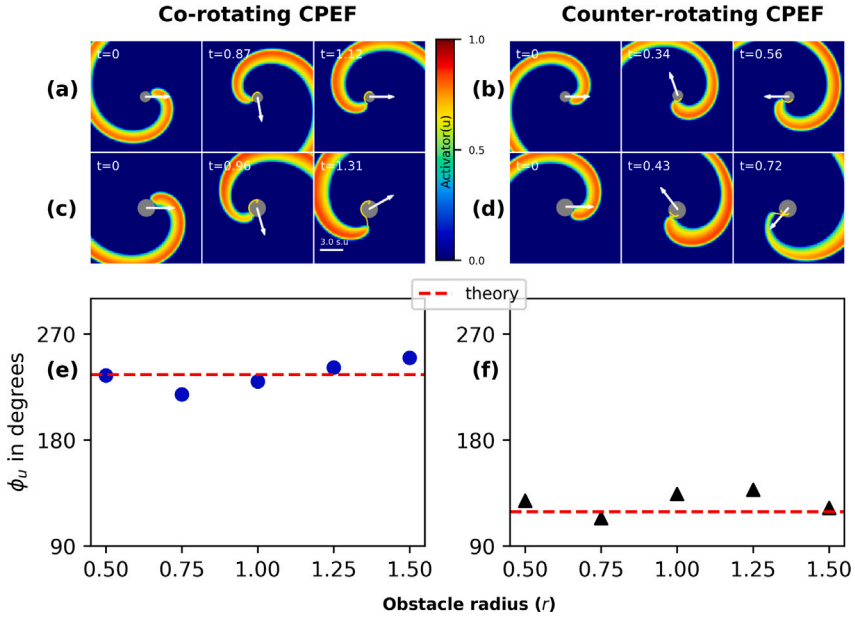

Fig. D.16. Unpinning of spiral pinned to varying obstacle sizes. In simulations, unpinning trials were conducted for co-rotating CPEF and counter-rotating CPEF at $\phi_0 = 45°$ and $p = 1.5$. The electric field strength is $E = 1.3\ E_{th}$. The **(a)** and **(b)** correspond to spiral unpinning from obstacle radius, $r = 0.75$ at $E = 0.5$, and **(c)** and **(d)** corresponds to the same for $r = 1.25$ at $E = 1.0$, respectively. We varied obstacle radius from $r = 0.5$ to $r = 1.5$ in steps of 0.25 and found the unpinning angle, ϕ_u, for **(e)** co-rotating CPEF and **(f)** counter-rotating CPEF. The simulation data is compared to the theoretical curve shown with the dotted line. The value of ϕ_u remained consistent regardless of obstacle radius in the simulations.

References

[1] Zaikin A, Zhabotinsky A. Concentration wave propagation in two-dimensional liquid-phase self-oscillating system. Nature 1970;225(5232):535–7.

[2] Barzykina I. Chemistry and mathematics of the Belousov–Zhabotinsky reaction in a school laboratory. J Chem Educ 2020;97(7):1895–902.

[3] Zhai C, Sun W. Analytical approximation of a self-oscillatory reaction system using the Laplace-Borel transform. Chaos Solitons Fractals 2021;142:110508.

[4] Gray C. An analysis of the belousov-zhabotinskii reaction. Rose-Hulman Undergraduate Math J 2002;3(1):1.

[5] Veeresha P. The efficient fractional order based approach to analyze chemical reaction associated with pattern formation. Chaos Solitons Fractals 2022;165:112862.

[6] Seipel M, Schneider FW, Münster AF. Control and coupling of spiral waves in excitable media. Faraday Discuss 2002;120:395–405.

[7] Zhang Y, Wu F, Wang C, Ma J. Stability of target waves in excitable media under electromagnetic induction and radiation. Phys A 2019;521:519–30.

[8] Bugrim AE, Dolnik M, Zhabotinsky AM, Epstein IR. Heterogeneous sources of target patterns in reaction- diffusion systems. J Phys Chem 1996;100(49):19017–22.

[9] Vanag VK, Epstein IR. Inwardly rotating spiral waves in a reaction-diffusion system. Science 2001;294(5543):835–7.
[10] Vanag VK, Epstein IR. Packet waves in a reaction-diffusion system. Phys Rev Lett 2002;88(8):088303.
[11] Davidenko JM, Pertsov AV, Salomonsz R, Baxter W, Jalife J. Stationary and drifting spiral waves of excitation in isolated cardiac muscle. Nature 1992;355(6358):349–51.
[12] Diagne K, Bury TM, Deyell MW, Laksman Z, Shrier A, Bub G, et al. Rhythms from two competing periodic sources embedded in an excitable medium. Phys Rev Lett 2023;130(2):028401.
[13] Zhang Y, Guo S, Sun M, Mariniello L, Tozzi A, Zhao X. Front waves of chemical reactions and travelling waves of neural activity. J NeuroPhilos 2022;1(2):222–39.
[14] Gorelova N, Bureš J. Spiral waves of spreading depression in the isolated chicken retina. J Neurobiol 1983;14(5):353–63.
[15] Siegert F, Weijer C. Digital image processing of optical density wave propagation in dictyostelium discoideum and analysis of the effects of caffeine and ammonia. J Cell Sci 1989;93(2):325–35.
[16] Kamino K, Kondo Y, Nakajima A, Honda-Kitahara M, Kaneko K, Sawai S. Fold-change detection and scale invariance of cell–cell signaling in social amoeba. Proc Natl Acad Sci 2017;114(21):E4149–57.
[17] Adamatzky A, de Lacy Costello B, Melhuish C, Ratcliffe N. Experimental implementation of mobile robot taxis with onboard belousov–zhabotinsky chemical medium. Mater Sci Eng C 2004;24(4):541–8.
[18] Parrilla-Gutierrez JM, Sharma A, Tsuda S, Cooper GJ, Aragon-Camarasa G, Donkers K, et al. A programmable chemical computer with memory and pattern recognition. Nat Commun 2020;11(1):1442.
[19] Adamatzky A. Collision-based computing in Belousov–Zhabotinsky medium. Chaos Solitons Fractals 2004;21(5):1259–64.
[20] Adamatzky A, de Lacy Costello B. Binary collisions between wave-fragments in a sub-excitable Belousov–Zhabotinsky medium. Chaos Solitons Fractals 2007;34(2):307–15.
[21] Toth R, Stone C, Adamatzky A, de Lacy Costello B, Bull L. Dynamic control and information processing in the Belousov–Zhabotinsky reaction using a coevolutionary algorithm. J Chem Phys 2008;129(18):184708.
[22] Kuksenok O, Yashin VV, Balazs AC. Mechanically induced chemical oscillations and motion in responsive gels. Soft Matter 2007;3(9):1138–44.
[23] Zykov VS. Spiral wave initiation in excitable media. Phil Trans R Soc A 2018;376(2135):20170379.
[24] Bittihn P, Squires A, Luther G, Bodenschatz E, Krinsky V, Parlitz U, et al. Phase-resolved analysis of the susceptibility of pinned spiral waves to far-field pacing in a two-dimensional model of excitable media. Philos Trans R Soc London A 2010;368(1918):2221–36.
[25] Fenton FH, Cherry EM, Hastings HM, Evans SJ. Multiple mechanisms of spiral wave breakup in a model of cardiac electrical activity. Chaos 2002;12(3):852–92.
[26] Traub RD, Wong RK. Cellular mechanism of neuronal synchronization in epilepsy. Science 1982;216(4547):745–7.
[27] Punacha S, Berg S, Sebastian A, Krinski VI, Luther S, Shajahan T. Spiral wave unpinning facilitated by wave emitting sites in cardiac monolayers. Proc R Soc A 2019;475(2230):20190420.
[28] Hussaini S, Venkatesan V, Biasci V, Romero Sepúlveda JM, Quiñonez Uribe RA, Sacconi L, et al. Drift and termination of spiral waves in optogenetically modified cardiac tissue at sub-threshold illumination. Elife 2021;10:e59954.
[29] Feng X, Gao X, Pan D-B, Li B-W, Zhang H. Unpinning of rotating spiral waves in cardiac tissues by circularly polarized electric fields. Sci Rep 2014;4:4831.
[30] Boccia E, Luther S, Parlitz U. Modelling far field pacing for terminating spiral waves pinned to ischaemic heterogeneities in cardiac tissue. Phil Trans R Soc A 2017;375(2096):20160289.
[31] Lilienkamp T, Parlitz U, Luther S. Taming cardiac arrhythmias: Terminating spiral wave chaos by adaptive deceleration pacing. Chaos 2022;32(12):121105.
[32] Buran P, Niedermayer T, Bär M. Mechanism of defibrillation of cardiac tissue by periodic low-energy pacing. bioRxiv 2023.
[33] Feng X, Yin X, Wen J, Wu H, Gao X. Removal of spiral turbulence by virtual electrodes through the use of a circularly polarized electric field. Chaos 2022;32(9):093145.
[34] Ma J, Jia Y, Yi M, Tang J, Xia Y-F. Suppression of spiral wave and turbulence by using amplitude restriction of variable in a local square area. Chaos Solitons Fractals 2009;41(3):1331–9.
[35] Ding Q, Wu Y, Hu Y, Liu C, Hu X, Jia Y. Tracing the elimination of reentry spiral waves in defibrillation: Temperature effects. Chaos Solitons Fractals 2023;174:113760.
[36] Aron M, Lilienkamp T, Luther S, Parlitz U. Optimising low-energy defibrillation in 2D cardiac tissue with a genetic algorithm. Front Netw Physiol 2023;3:1172454.
[37] Sutthiopad M, Luengviriya J, Porjai P, Phantu M, Kanchanawarin J, Müller SC, et al. Propagation of spiral waves pinned to circular and rectangular obstacles. Phys Rev E 2015;91(5):052912.
[38] El-Nabulsi RA, Anukool W. Spiral waves in fractal dimensions and their elimination in λ- ω systems with less damaging intervention. Chaos Solitons Fractals 2024;178:114317.
[39] Howell L, Osborne E, Franklin A, Hébrard É. Pattern recognition of chemical waves: Finding the activation energy of the autocatalytic step in the Belousov–Zhabotinsky reaction. J Phys Chem B 2021;125(6):1667–73.
[40] Körös E, Orbán M. Uncatalysed oscillatory chemical reactions. Nature 1978;273(5661):371–2.
[41] Sakurai T, Mihaliuk E, Chirila F, Showalter K. Design and control of wave propagation patterns in excitable media. Science 2002;296(5575):2009–12.
[42] Kuhnert L, Agladze K, Krinsky V. Image processing using light-sensitive chemical waves. Nature 1989;337(6204):244–7.
[43] Munuzuri A, Innocenti C, Flesselles J-M, Gilli J-M, Agladze K, Krinsky V. Elastic excitable medium. Phys Rev E 1994;50(2):R667.
[44] Kalishyn YY, Rachwalska M, Strizhak PE. Stirring effect on the Belousov-Zhabotinsky oscillating chemical reactions in a batch. experimental and modelling. Z Naturforschung A 2010;65(1–2):132–40.
[45] Karimov A, Kopets E, Karimov T, Almjasheva O, Arlyapov V, Butusov D. Empirically developed model of the stirring-controlled Belousov–Zhabotinsky reaction. Chaos Solitons Fractals 2023;176:114149.
[46] Steinbock O, Zykov V, Müller SC. Control of spiral-wave dynamics in active media by periodic modulation of excitability. Nature 1993;366(6453):322–4.
[47] Agladze K, De Kepper P. Influence of electric field on rotating spiral waves in the Belousov-Zhabotinskii reaction. J Phys Chem 1992;96(13):5239–42.
[48] Steinbock O, Schütze J, Müller S. Electric-field-induced drift and deformation of spiral waves in an excitable medium. Phys Rev Lett 1992;68(2):248.
[49] Hu Y, Ding Q, Wu Y, Jia Y. Polarized electric field-induced drift of spiral waves in discontinuous cardiac media. Chaos Solitons Fractals 2023;175:113957.
[50] Li T-C, Gao X, Zheng F-F, Pan D-B, Zheng B, Zhang H. A theory for spiral wave drift induced by ac and polarized electric fields in chemical excitable media. Sci Rep 2017;7(1):1–9.
[51] Chen J-X, Zhang H, Li Y-Q. Drift of spiral waves controlled by a polarized electric field. J Chem Phys 2006;124(1):014505.
[52] Chen J-X, Zhang H, Li Y-Q. Synchronization of a spiral by a circularly polarized electric field in reaction-diffusion systems. J Chem Phys 2009;130(12):124510.
[53] Li B-W, Cai M-C, Zhang H, Panfilov AV, Dierckx H. Chiral selection and frequency response of spiral waves in reaction-diffusion systems under a chiral electric field. J Chem Phys 2014;140(18):184901.
[54] Ji L, Zhou Y, Li Q, Qiao C, Ouyang Q. Experimental evidence of using a circularly polarized electric field to control spiral turbulence. Phys Rev E 2013;88(4):042919.
[55] Sutthiopad M, Luengviriya J, Porjai P, Tomapatanaget B, Müller SC, Luengviriya C. Unpinning of spiral waves by electrical forcing in excitable chemical media. Phys Rev E 2014;89(5):052902.
[56] Amrutha S, Sebastian A, Sibeesh P, Punacha S, Shajahan T. Mechanism of spiral wave unpinning in the Belousov–Zhabotinsky reaction with a DC electric field. J Phys Chem C 2022;126(46):19618–26.
[57] Amrutha S, Sebastian A, Sibeesh P, Punacha S, Shajahan T. Theory and experiments of spiral unpinning in the Belousov–Zhabotinsky reaction using a circularly polarized electric field. Chaos 2023;33(6):063157.
[58] Punacha S, Kumara N, Shajahan T. Theory of unpinning of spiral waves using circularly polarized electric fields in mathematical models of excitable media. Phys Rev E 2020;102(3):032411.
[59] Sibeesh P, Shajahan T. Image acquisition and electric field application in the Belousov-Zhabotinsky reaction using LabVIEW. In: Springer proceedings in physics. Springer; 2024, in press.
[60] Keener JP, Tyson JJ. Spiral waves in the Belousov-Zhabotinskii reaction. Physica D 1986;21(2–3):307–24.
[61] Field RJ, Noyes RM. Oscillations in chemical systems. IV. Limit cycle behavior in a model of a real chemical reaction. J Chem Phys 1974;60(5):1877–84.
[62] Fenton FH, Cherry EM, Karma A, Rappel W-J. Modeling wave propagation in realistic heart geometries using the phase-field method. Chaos 2005;15(1):013502.
[63] Li B-W, Deng L-Y, Zhang H. Chiral symmetry breaking in a reaction-diffusion system. Phys Rev E 2013;87(4):042905.
[64] Deng L-Y, Zhang H, Li Y-Q. Stabilization of multiarmed spiral waves by circularly polarized electric fields. Phys Rev E 2009;79(3):036107.
[65] Pumir A, Krinsky V. Unpinning of a rotating wave in cardiac muscle by an electric field. J Theoret Biol 1999;199(3):311–9.
[66] Hornung D, Biktashev V, Otani N, Shajahan T, Baig T, Berg S, et al. Mechanisms of vortices termination in the cardiac muscle. R Soc Open Sci 2017;4(3):170024.
[67] Back O, Asally M, Wang Z, Hayashi Y. Electrotaxis behavior of droplets composed of aqueous Belousov-Zhabotinsky solutions suspended in oil phase. Sci Rep 2023;13(1):1340.
[68] Sharma A, Ng MT-K, Parrilla Gutierrez JM, Jiang Y, Cronin L. A programmable hybrid digital chemical information processor based on the Belousov-Zhabotinsky reaction. Nature Commun 2024;15(1):1984.